This item is the archived peer-reviewed author-version of:

Atomic-scale detection of individual lead clusters confined in Linde Type A zeolites

ARTICLE

Atomic-Scale Detection of Individual Lead Clusters Confined in Linde Type A Zeolites

Jarmo Fatermans[‡a,b], Giacomo Romolini[‡d], Thomas Altantzis[‡a,b,c], Johan Hofkens[d,e], Maarten B. J. Roeffaers[*f], Sara Bals[a,b], and Sandra Van Aert[*a,b]

Structural analysis of metal clusters confined in nanoporous materials is typically performed by X-ray-driven techniques. Although X-ray analysis has proved its strength in the characterization of metal clusters, it provides averaged structural information. Therefore, we here present an alternative workflow for bringing the characterization of confined metal clusters towards the local scale. This workflow is based on the combination of aberration-corrected transmission electron microscopy (TEM), TEM image simulations, and powder X-ray diffraction (XRD) with advanced statistical techniques. In this manner, we were able to characterize the clustering of Pb atoms in Linde Type A (LTA) zeolites with Pb loadings as low as 5 wt%. Moreover, individual Pb clusters could be directly detected. The proposed methodology thus enables a local-scale characterization of confined metal clusters in zeolites. This is important for further elucidation of the connection between the structure and the physicochemical properties of such systems.

Introduction

Small metal clusters with sub-nm dimensions form a class of interesting materials that show completely different physicochemical properties as compared to corresponding single metal atoms or nanoparticles, as well as to their bulk counterparts. In particular, their luminescence properties[1–6] and high catalytic activity[7,8] stand out. These remarkable properties arise from discrete energy levels in the electronic structure of the clusters since they consist of only a few metal atoms bonded together.[9] However, sub-nm metal clusters are extremely unstable due to their high surface energy. Therefore, a stabilizing agent is essential to avoid their coagulation and several solutions have been proposed, from DNA[10,11] and polymers[12] to inorganic matrices such as glasses[13] and zeolites.[14–17]

In order to understand the relation between the physicochemical properties of sub-nm confined metal clusters and their atomic structure, detailed structural characterization is required. Typical methods to unravel the geometry of metal clusters are based on X-ray-driven techniques such as X-ray diffraction (XRD) and X-ray absorption spectroscopy (XAS).[18–23] Among XAS techniques, extended X-ray absorption fine structure (EXAFS) is a popular technique that directly probes the local environment of a specific element. However, EXAFS sensitivity for distinguishing different clusters with identical chemical composition is not optimal due to its unselective nature towards other species containing the same probed element. In addition, EXAFS suffers from complex data analysis in which theoretical modeling with a priori knowledge of the sample is often necessary. Although these X-ray based techniques are powerful tools for structure determination, they only provide averaged structural information. Therefore, alternative structure characterization techniques are crucial to locally identify clusters and to avoid this averaging effect.

Aberration-corrected high-resolution transmission electron microscopy (TEM) is an extremely useful imaging technique that can overcome the limitations posed by X-ray analysis for investigating confined sub-nm metal clusters at the atomic scale. More specifically, high-angle annular dark-field (HAADF) scanning transmission electron microscopy (STEM) is of interest because of its strong dependence on the atomic number.[24,25] As a result, heavier atoms appear brighter as compared to lighter ones in HAADF STEM images, which is ideal to locate clusters in a zeolite framework. However, in order to connect the structure of the clusters to their properties, one needs to perform a quantitative interpretation of these images, which is far from straightforward given the sensitivity of zeolites towards the electron beam. Such investigations will be even more challenging for small loadings.

In this paper, we will therefore design a dedicated statistical approach that will enable us to decide on the presence of metal nanoclusters in specific cages of a zeolite. The ability to extract such local information reliably and directly is of great

a. Electron Microscopy for Materials Science (EMAT), University of Antwerp, Groenenborgerlaan 171, 2020 Antwerp, Belgium. E-mail: sandra.vanaert@uantwerpen.be

b. NANOlab Center of Excellence, University of Antwerp, Belgium. E-mail: sandra.vanaert@uantwerpen.be

c. Applied Electrochemistry and Catalysis Group (ELCAT), University of Antwerp, Universiteitsplein 1, 2610 Wilrijk, Belgium.

d. Molecular Imaging and Photonics, Department of Chemistry, KU Leuven, Celestijnenlaan 200F, 3001 Leuven, Belgium.

e. Max Planck Institute for Polymer Research, Ackermannweg 10, 55128 Mainz, Germany.

f. Centre for Membrane Separations, Adsorption, Catalysis, And Spectroscopy for Sustainable Solutions (cMACS), KU Leuven, Celestijnenlaan 200F, Box 2461, 3001, Leuven, Belgium. E-mail: maarten.roeffaers@kuleuven.be

‡ These authors contributed equally to this work.

Electronic Supplementary Information (ESI) available. See DOI: 10.1039/x0xx00000x

importance and will enable the further rational design of these systems.

Results and discussion

Figure 1 illustrates examples of high-resolution HAADF STEM micrographs of Pb-loaded Linde Type A (LTA) zeolites with different amounts of Pb loadings imaged along the [100] zone axis. Figure 1(a) depicts an over-exchanged Pb-LTA zeolite (Pb$_{full}$-LTA), where an abundance of Pb^{2+} ions has replaced the Na$^+$ ions. In Figures 1(b) and (c), ~10wt% and ~5wt% of Pb have been incorporated within the zeolite framework, respectively. These samples are referred to as Pb$_1$-LTA and Pb$_{0.5}$-LTA systems and they contain theoretically 1 and 0.5 Pb^{2+} ions per normalized unit cell (NUC), respectively. These values were determined by inductively coupled plasma – mass spectrometry (ICP-MS) and atomic absorption spectroscopy (AAS).[22] For clarity, Figure 1(d) shows a schematic representation of the LTA zeolite structure along the [100] zone axis. Although HAADF STEM images give a first indication of the framework structure and the possible location of Pb atoms, a more quantitative interpretation is desirable. In order to evaluate the local concentration and distribution of Pb atoms inside the Pb-LTA zeolites, statistical parameter estimation theory can be used. This approach has been applied previously to HAADF STEM images for obtaining precise structural information.[26–29] Hereby, a fitting procedure is used to match a proposed parametric model with the observed raw image data. Typically, a superposition of Gaussian peaks, describing the atomic columns, is used as a parametric model for HAADF STEM images.[29] However, this non-linear optimization method requires starting values for the atomic column positions as an input. Good starting values are necessary in order to converge to the global optimum during the fitting procedure. From Figure 1, it is clear that this is not a straightforward task by only relying on the acquired raw HAADF STEM images of the Pb-zeolites since the signal-to-noise ratio (SNR) is not sufficient to resolve all atomic columns. Because of the beam sensitivity of LTA zeolites, containing a relatively low Si/Al ratio,[30] they are easily damaged by the high-energy electrons of the beam.[31,32] Therefore, the HAADF STEM images have been acquired with a low electron dose of around 600 e$^-$/Å^2 resulting in a low SNR and low contrast-to-noise ratio (CNR). When atomic columns in HAADF STEM images possess low CNR values, the perceived image quality becomes insufficient to reliably and directly recognize the atomic columns from the image data.[33,34] By making use of the periodicity of the zeolite framework, the CNR of the raw HAADF STEM image data can be improved. This improvement is achieved by applying a template-matching procedure,[30] of which the results are shown in the insets of Figure 1. More details on the technique of template matching can be found in the Supplementary Information. From the template-matched images, the distinction between the sodalite (SOD) cages and supercages of the LTA zeolite becomes apparent. Moreover, the template-matched images allow aligning the atomic column positions following from complementary powder XRD measurements to the HAADF STEM image data. This has been illustrated in Figure S2. As such, since template-matched images are constructed by averaging similar regions, suitable atomic column locations can be provided for the raw image data, enabling quantitative analysis of the Pb-zeolites at the local scale by model fitting. More details on the powder XRD analysis and the parametric fitting procedure are provided in the experimental section (vide infra).

Using model-based fitting, the total intensity of electrons scattered by each atomic column, the so-called scattering cross-section,[29,35,36] can be measured. By comparing the experimental scattering cross-sections with the theoretical ones obtained from image simulations,[37] the number of Pb atoms confined within the zeolite framework can be determined at a local scale. A distinction has been made between the different types of Pb positions that are present in Pb-LTA zeolites determined by XRD structure refinement. The different Pb positions, namely Pb-1, Pb-2, Pb-3, and Pb-4, are displayed in Figure 2(a), showing the Pb-LTA zeolite unit cell (UC) along the [100] direction.

The luminescence properties of Pb-LTA zeolites have been attributed to the formation of small Pb clusters in the SOD cages.[22] Hereby, an unusual short Pb-Pb distance of ca. 2.9 Å has been reported.[22] From XRD, the Pb-1 − Pb-1 and Pb-3 − Pb-3 distances are estimated to be ca. 5.3 Å and 6.0 Å, respectively, which are too large for atomic interaction. Furthermore, the Pb-1 and Pb-3 atoms are not located inside the SOD cage, but on the central plane of the six-membered rings composing the SOD cages. The distance between Pb atoms in the Pb-2 positions, though, is estimated to be ca. 2.8 Å, which corresponds well to the reported cluster Pb-Pb distance of 2.9 Å. This observed deviation between the estimated positions of the atoms of the clusters and the reported Pb-2 locations results from the unavoidable presence of noise in the low dose recorded images and the use of a relatively large pixel size of 0.485 Å. Therefore, Pb atoms related to the formation of Pb-clusters can be attributed reasonably well to Pb-2 positions.

Figure 2(b) shows the scattering cross-sections obtained from image simulations of a Pb-2 type column, which is located inside the SOD cages (see Figure 2(a)), as a function of the number of Pb atoms within the column for varying sample thickness. As expected for HAADF STEM, a monotonically increasing relationship is observed in Figure 2(b).[38] In Figure S4, similar plots can be found for the Pb-1 and Pb-3 column positions. In this quantification, the effect of the complex and dense network of the Si, Al, and O atoms of the zeolite framework, and the remaining Na atoms on the cross-sections of the Pb atoms is taken into account. This is explained in more detail in the Supplementary Information. Next, by comparing the experimentally measured cross-sections with simulated ones, the number of Pb atoms along the viewing direction in each atomic column can be determined for the different types of Pb positions. Hereby, local thickness variations have been determined from adjacent Si/Al columns. In Figure S2, the positions of Si/Al columns are shown. More details on the thickness-estimation process can be found in the Supplementary Information. Figures 2(c) and (d), which correspond to Figures 1(a) and (b), display the results of the atom-counting procedure for HAADF STEM images of the Pb$_1$-

LTA and $Pb_{0.5}$-LTA zeolite samples, respectively. For clarity, only the total number of Pb atoms observed within the projected SOD cages is presented. In Figures S5 and S6, more detailed representations of the atom-counting results for the Pb columns are shown. The total number of Pb atoms (see Figure 2) in combination with estimates of the sample thickness (see Figure S7), and thus the number of UCs, can be used to calculate the number of Pb^{2+} cations per NUC for the Pb_1-LTA and $Pb_{0.5}$-LTA samples. It follows that this number equals 1.14 for the Pb_1-LTA zeolite, where a theoretical number of 1 is expected. For the $Pb_{0.5}$-LTA zeolite, the number of Pb^{2+} cations per NUC equals 0.72, as compared to a theoretical value of 0.5. These measured Pb concentrations are comparable to measurements performed with spectroscopic techniques.[22] From the Pb concentration measurements, it is confirmed that the Pb_1-LTA zeolite sample contains more Pb than the $Pb_{0.5}$-LTA sample, as expected. This provides confidence in the reliability of the thicknesses and number of Pb atoms obtained from the STEM images by the described methodology.

Interestingly, local Pb variations can be observed from Figures 2(c) and (d) indicating that certain projected SOD cages contain considerably more Pb atoms than other cages. However, a statistical approach is required to investigate whether these inhomogeneities in the Pb concentration are due to a physical tendency of Pb atoms to cluster together or due to a mere random process.[22] Therefore, the focus of this statistical investigation lies on the Pb-2 atoms, which are located inside the SOD cages as shown in Figure 2(a) and are responsible for the cluster formation as mentioned earlier. If the Pb atoms would be randomly distributed over the SOD cages, one would expect the number of Pb atoms observed along projected SOD cages with comparable thicknesses to be Poisson distributed. A deviation from the Poisson distribution is an indication that the Pb atoms are not just randomly positioned in the zeolite, but that a clustering effect takes place. The histograms in Figures 3(a)-(d) display the distributions of the number of Pb-2 atoms counted along the [100] direction of SOD cages with different thicknesses of the Pb_1-LTA sample. These histograms are then compared with the expected Poisson distributions shown in red. Statistical hypothesis testing has been used to confirm that the observed distributions of the number of Pb atoms deviate from a Poisson distribution.[39] More technical details on statistical hypothesis testing are provided in the Supplementary Information. The deviation is most pronounced in the tails of the distributions, which are enlarged in the insets of Figure 3, showing the presence of a relatively large number of Pb-2 atoms in some projected SOD cages. This is an indication of the occurrence of Pb clustering inside the SOD cages of the LTA zeolite. In Figures 3(e)-(h), similar plots are shown for the $Pb_{0.5}$-LTA zeolite sample. From these figures, similar conclusions can be drawn. This analysis confirms that the observed distributions of Pb-2 atoms, throughout the Pb_1-LTA and $Pb_{0.5}$-LTA samples, are due to a physical tendency of Pb atoms clustering together in the SOD cages.

Ideally, the acquired HAADF STEM image data may be used to detect individual tetrahedral Pb-clusters inside the SOD cages of the zeolite samples at the local scale. Unfortunately, this is not a straightforward task because only a limited number of cages actually contain clusters. In an ideal case, under the assumption that all the Pb-2 atoms form clusters, still only around 4 % of the SOD cages are expected to host Pb-clusters in both Pb_1-LTA and $Pb_{0.5}$-LTA samples (vide infra for occupancy analysis). This percentage follows from the analysis of the HAADF STEM image data. In addition, the projected two-dimensional HAADF STEM images lack clear information along the third dimension regarding the depth location of the Pb atoms and the beam sensitivity of LTA zeolites does not allow for a three-dimensional study by, for example, electron tomography. Nevertheless, in Figure 4, possible locations of tetrahedral Pb-clusters throughout the $Pb_{0.5}$-LTA zeolite sample have been highlighted. The estimated thicknesses at these locations were found to be 4.0 nm and 5.9 nm, corresponding to roughly two UCs. It can therefore be assumed that the indicated Pb atoms are located at a similar depth location in the LTA-zeolite, thus forming tetrahedral Pb-clusters.

Interestingly, besides the confirmation of a clustering tendency, the occupancies of the Pb atoms throughout the Pb_1-LTA and $Pb_{0.5}$-LTA samples can also be estimated. Although XRD could not be used to measure the occupancies of the Pb-1, Pb-2, Pb-3, and Pb-4 positions for these samples because of the low Pb loadings, these can be obtained from the HAADF STEM results. Indeed, from the estimated thickness and Pb-counting results, one can determine how many of the available Pb positions do contain Pb atoms. Table 1 shows the occupancy factors for the Pb_1-LTA and $Pb_{0.5}$-LTA samples, normalized by their sum. These occupancy values are determined by considering the local amount of counted Pb atoms and the local zeolite thickness. This approach is more intuitive and direct as compared to an average template-matched procedure. The latter approach would not yield any information on local cluster formation, one of the goals of this work. In addition, knowledge on local zeolite thickness variations would be lost as well, leading to less accurate site occupancy estimates. The uncertainties on occupancies, calculated from HAADF STEM images, follow from uncertainties in the atom counting results of the individual columns (see Supplementary Information). To confirm the validity of occupancy calculations from HAADF STEM images, occupancy values were also obtained from Rietveld refinement for the Pb_{full}-LTA sample. Also in this case, normalized occupancies were used in order to be directly comparable to those obtained from our HAADF STEM analysis. As reported in table 1, the differences between HAADF STEM and XRD occupancies are equal to or lower than 20%, indicating a good agreement between the two techniques and confirming the validity of the developed method.

The measured occupancies may give further insight into the mechanism of the observed luminescence in Pb-LTA zeolites. It has been reported that the $Pb_{0.5}$-LTA zeolite possesses a stronger luminescence intensity as compared to the Pb_1-LTA zeolite.[22] From Table 1 and Fig. 5, it can be seen that the normalized occupancies of the Pb-2 positions for Pb1-LTA and Pb0.5-LTA zeolites differ noticeably. This suggests a higher number of luminescent clusters confined within the SOD cages of the **Pb0.5**-LTA sample. This implies that for an increased Pb

loading, the additional Pb atoms do not show the initial tendency of further occupying the Pb-2 positions, but rather occupy Pb-1 and Pb-3 positions. Indeed, the occupancy factors of the Pb-1 and Pb-3 positions are significantly larger for the Pb1-LTA sample as compared to the Pb0.5-LTA sample and even larger for Pbfull-LTA. This means that there is a higher amount of Pb atoms present at the borders of the SOD cages in the Pb1-LTA zeolite, possibly quenching the luminescence of clusters inside the SOD cages. These local insights might trigger the further optimization of the luminescence properties of these systems.

Conclusions

In this work, by applying aberration-corrected HAADF STEM in combination with image simulations, powder XRD measurements, and advanced statistical techniques, the Pb concentration and clustering within Pb-LTA zeolites with Pb loadings as low as 5 wt% could be quantitatively analyzed at a local scale. Such a detailed and precise characterization was achieved despite the electron-beam sensitivity of the zeolite samples which causes the HAADF STEM data acquisition to be performed at a limited incident electron dose, resulting in images with low SNR. It was revealed that intensity variations between the image data of the Pb_1-LTA and $Pb_{0.5}$-LTA samples are indeed related to a different amount of Pb atoms present in the zeolite framework. Furthermore, Pb concentrations in the Pb_1-LTA and $Pb_{0.5}$-LTA zeolites could be successfully measured. Moreover, by statistical analysis, it could be proven that the Pb atoms have a physical tendency of clustering together inside the SOD cages of the zeolite framework, forming tetrahedral Pb-clusters which are responsible for the luminescence properties of Pb-LTA zeolites. Interestingly, even the occupancies of Pb positions within the low Pb-loaded samples could be extracted from HAADF STEM, which is not achievable from XRD, and which may contribute to the understanding of the improved luminescence properties of $Pb_{0.5}$-LTA zeolites as compared to Pb_1-LTA zeolites as more information is provided on how the Pb atoms are distributed over the different position types. Finally, it has been shown that HAADF STEM even allows to detect specific locations where possible Pb clusters are formed. The methodology described in this work is a first achievement of bringing the characterization of small, confined metal clusters towards the local scale. This is important for studying the exact atomic-scale organization of these clusters and for further elucidating the origins of their interesting physicochemical properties.

Experimental details and methods

Sample preparation

Pb clusters were prepared in a commercial LTA zeolite after an ion-exchange process, where Pb^{2+} ions replaced Na^+ ions, and a thermal treatment. Although the synthesis procedure of confining Pb clusters in LTA zeolites has been thoroughly described in previous work,[22] a brief description will be given

here. Sample preparation started by dispersing 500 mg of a commercial LTA zeolite (from UOP Honeywell) in 100 ml of a $7,33 \cdot 10^{-4}$ M or $1,47 \cdot 10^{-3}$ M $Pb(NO_3)_2$ (Sigma-Aldrich, ≥ 99.0 %) solution. The concentration of $Pb(NO_3)_2$ has been chosen so to have 0.5 or 1 Pb^{2+} ions per NUC in the final Pb-LTA zeolite sample, exhibiting the highest photoluminescence quantum yield (PLQY).[22] These samples are referred to as a $Pb_{0.5}$-LTA and Pb_1-LTA zeolite, respectively. In general, the notation of Pb_x-LTA denotes the theoretical Pb content of the zeolite, meaning that on average x Pb^{2+} cations per NUC, with a dry chemical composition of $Pb_xNa_{12-2x}Si_{12}Al_{12}O_{48}$, have been exchanged. The sample was left overnight in an end-over-end shaker for homogenous agitation in darkness. The following day, the sample was recovered by filtration and washed several times with ultrapure H_2O. The recovered powder was then dried at 353 K to remove the excess of water. After that, the dried sample was transferred into a muffle and heated with a step-heating program that heats at 353 K for 30 min, then, at 383 K for another 30 min, and, finally, it heats at 723 K overnight. Hereby, the temperature ramp was 5 K/min. At last, the sample was transferred into a desiccator, containing a saturated solution of K_2SO_4 that ensures 98 % of humidity, in order to obtain a fully hydrated sample.

TEM setup description

An aberration-corrected ThermoFischer Scientific Titan transmission electron microscope has been used to acquire high-resolution HAADF STEM images. Hereby, the acceleration voltage was set to 300 kV and the frame size for each acquisition was 1024 × 1024 pixels using a dwell time of 1 μs. The beam current has been estimated to be around 23 pA. Furthermore, in order to enable a quantitative comparison with simulations, the experimental images have been normalized with respect to the incident beam by acquiring a detector scan.[40]

TEM image simulation

Simulated high-resolution HAADF STEM images have been obtained by applying the MULTEM software,[41,42] using input values in correspondence to the experimental microscope settings. Hereby, detector sensitivity and source-size broadening with a full width at half maximum (FWHM) of 0.7 Å have been taken into account. The input structure of the Pb-LTA zeolite has been derived from XRD analysis. A complete list of simulation parameters is displayed in Table S2.

HAADF STEM image quantification

The experimental and simulated high-resolution HAADF STEM images have been described by a parametric model, consisting of a superposition of Gaussian functions which are peaked at the atomic column positions. By fitting this model to the image data by a least-squares estimator, estimates of the peak intensities and widths of the atomic columns could be obtained, from which estimates of the column cross-sections followed.[29,35,36] Model fitting has been performed on the level of individual raw template regions. In order to determine the number of atoms within the SOD cages, image simulations of

the different kinds of Pb columns have been performed while varying the amount of Pb atoms within the column. Hereby, the Pb atoms have been positioned at the top of the column. The obtained simulated values for the cross-sections of the Pb columns can then be compared to the observed cross-sections in the experimental data in order to perform atom counting.[37]

Powder XRD measurements

X-ray diffractograms were measured at the European Synchrotron Radiation Facility (ESRF) at the Swiss-Norwegian beamline 01 (BM01) for an over-exchanged Pb-LTA zeolite in fully hydrated form. The over-exchanged Pb-LTA zeolite was prepared similarly as the Pb_1-LTA and $Pb_{0.5}$-LTA samples, however, the exchange was performed using an excess of $Pb(NO_3)_2$ in order to fully replace the Na^+ atoms. The fully hydrated sample was loaded and sealed in a glass capillary with a diameter of 0.5 mm. The data were collected using an X-ray wavelength of 0.72310 Å, using a PILATUS 2M detector in the region $2\theta = 0°$ to $50°$. The step size was $0.01°$ and an integration time of 30 s was used. Rietveld analysis was performed with FullProf software.[43] Hereby, the starting model for structural refinement was taken from Ronay & Seff.[19] In table S1, the occupancy factors of the Pb positions within an over-exchanged Pb-LTA are displayed. It is noted that similar measurements on LTA zeolites with lower Pb loadings are not achievable because then the Pb concentration is too low to be probed with XRD.

Author Contributions

J.F, G.R, and T.A contributed equally. G.R prepared the samples, performed photoluminescence and XRD characterization under supervision of M.B.J.R. and J.H. T.A. acquired the experimental HAADF STEM image data under supervision of S.B. J.F. performed the data analysis and HAADF STEM simulations under supervision of S.V.A. The manuscript was written through contributions of all authors. All authors have given approval to the final version of the manuscript.

Conflicts of interest

There are no conflicts to declare.

Acknowledgements

References

1   G. De Cremer, E. Coutiño-Gonzalez, M. B. J. Roeffaers, B. Moens, J. Ollevier, M. Van der Auweraer, R. Schoonheydt, P. A. Jacobs, F. C. De Schryver, J. Hofkens, D. E. De Vos, B. F. Sels and T. Vosch, *J. Am. Chem. Soc.*, 2009, **131**, 3049–3056.

2   E. Coutino-Gonzalez, M. B. J. Roeffaers, B. Dieu, G. De Cremer, S. Leyre, P. Hanselaer, W. Fyen, B. Sels and J. Hofkens, *J. Phys. Chem. C*, 2013, **117**, 6998–7004.

3   N. Goswami, Q. Yao, Z. Luo, J. Li, T. Chen and J. Xie, *J. Phys. Chem. Lett.*, 2016, **7**, 962–975.

4   E. Coutiño-Gonzalez, W. Baekelant, J. A. Steele, C. W. Kim, M. B. J. Roeffaers and J. Hofkens, *Acc. Chem. Res.*, 2017, **50**, 2353–2361.

5   Z. Han, X. Y. Dong, P. Luo, S. Li, Z. Y. Wang, S. Q. Zang and T. C. W. Mak, *Sci. Adv.*, 2020, **6**, 1–9.

6   E. Coutino-Gonzalez, M. Roeffaers and J. Hofkens, 2020, pp. 75–103.

7   K. Shimizu, K. Sawabe and A. Satsuma, *Catal. Sci. Technol.*, 2011, **1**, 331.

8   S. Pramanik, V. Bhalla and M. Kumar, *Appl. Mater. Interfaces*, 2015, **7**, 22786–22795.

9   I. Díez and R. H. A. Ras, *Nanoscale*, 2011, **3**, 1963.

10   E. Gwinn, D. Schultz, S. Copp and S. Swasey, *Nanomaterials*, 2015, **5**, 180–207.

11   D. J. E. Huard, A. Demissie, D. Kim, D. Lewis, R. M. Dickson, J. T. Petty and R. L. Lieberman, *J. Am. Chem. Soc*, 2019, **141**, 114465–11470.

12   H. Xu and K. S. Suslick, *ACS Nano*, 2010, **4**, 3209–3214.

13   A. S. Kuznetsov, V. K. Tikhomirov, M. V. Shestakov and V. V. Moshchalkov, *Nanoscale*, 2013, **5**, 10065.

14   G. De Cremer, B. F. Sels, J. Hotta, M. B. J. Roeffaers, E. Bartholomeeusen, E. Coutiño-Gonzalez, V. Valtchev, D. E. De Vos, T. Vosch and J. Hofkens, *Adv. Mater.*, 2010, **22**, 957–960.

15   O. Fenwick, E. Coutiño-Gonzalez, D. Grandjean, W. Baekelant, F. Richard, S. Bonacchi, D. De Vos, P. Lievens, M. Roeffaers, J. Hofkens and P. Samorì, *Nat. Mater.*, 2016, **15**, 1017–1022.

16   D. Grandjean, E. Coutiño-Gonzalez, N. T. Cuong, E. Fron, W. Baekelant, S. Aghakhani, P. Schlexer, F. D'Acapito, D. Banerjee, M. B. J. Roeffaers, M. T. Nguyen, J. Hofkens and P. Lievens, *Science (80-.).*, 2018, **361**, 686–690.

17   W. Baekelant, S. Aghakhani, E. Coutino-Gonzalez, K. Kennes, F. D'Acapito, D. Grandjean, M. Van Der Auweraer, P. Lievens, M. B. J. Roeffaers, J. Hofkens and J. A. Steele, *J. Phys. Chem. Lett*, 2018, **9**, 5344–5350.

18   C. Ronay and K. Seff, *J. Phys. Chem.*, 1985, **89**, 1965–1970.

19   C. Ronay and K. Seff, *Zeolites*, 1993, **13**, 97–101.

20   E. Coutino-Gonzalez, D. Grandjean, M. Roeffaers, K. Kvashnina, E. Fron, B. Dieu, G. De Cremer, P. Lievens, B. Sels and J. Hofkens, *Chem. Commun.*, 2014, **50**, 1350–1352.

21   S. Aghakhani, D. Grandjean, W. Baekelant, E. Coutiño-Gonzalez, E. Fron, K. Kvashnina, M. B. J. Roeffaers, J. Hofkens, B. F. Sels and P. Lievens, *Nanoscale*, 2018, **10**, 11467–11476.

22   W. Baekelant, S. Aghakhani, E. Coutino-Gonzalez, D. Grandjean, K. Kennes, D. Jonckheere, E. Fron, F. D'Acapito, A. Longo, P. Lievens, M. B. J. Roeffaers and J. Hofkens, *J. Phys. Chem. C*, 2018, **122**, 13953–13961.

23   O. Fenwick, E. Coutiño-Gonzalez, F. Richard, S. Bonacchi, W. Baekelant, D. Vos, M. B. J. Roeffaers, J. Hofkens and P. Samorì, *Small*, 2020, **16**, 2002063.

24   S. J. Pennycook, *Annu. Rev. Mater. Sci.*, 1992, **22**, 171–195.

25   P. D. Nellist and S. J. Pennycook, 2000, pp. 147–203.

26   A. J. den Dekker, S. Van Aert, A. van den Bos and D. Van Dyck, *Ultramicroscopy*, 2005, **104**, 83–106.

27   S. Van Aert, A. J. den Dekker, A. van den Bos, D. Van Dyck and J. H. Chen, *Ultramicroscopy*, 2005, **104**, 107–125.

28   S. Van Aert, W. Van den Broek, P. Goos and D. Van Dyck, *Micron*, 2012, **43**, 509–515.

29   A. De Backer, K. H. W. van den Bos, W. Van den Broek, J. Sijbers and S. Van Aert, *Ultramicroscopy*, 2016, **171**, 104–116.

30   T. Altantzis, E. Coutino-Gonzalez, W. Baekelant, G. T. Martinez, A. M. Abakumov, G. Van Tendeloo, M. B. J. Roeffaers, S. Bals and J. Hofkens, *ACS Nano*, 2016, **10**, 7604–7611.

31   A. Mayoral, T. Carey, P. A. Anderson, A. Lubk and I. Diaz, *Angew. Chemie Int. Ed.*, 2011, **50**, 11230–11233.

32   A. Mayoral, T. Carey, P. A. Anderson and I. Diaz, *Microporous Mesoporous Mater.*, 2013, **166**, 117–122.

33   J. Fatermans, A. J. Den Dekker, K. Müller-Caspary, I. Lobato, C. M. O'Leary, P. D. Nellist and S. Van Aert, *Phys. Rev. Lett.*, 2018, **121**, 056101.

34   J. Fatermans, S. Van Aert and A. J. den Dekker, *Ultramicroscopy*, 2019, **201**, 81–91.

35   S. Van Aert, J. Verbeeck, R. Erni, S. Bals, M. Luysberg, D. Van Dyck and G. Van Tendeloo, *Ultramicroscopy*, 2009, **109**, 1236–1244.

36   H. E, K. E. MacArthur, T. J. Pennycook, E. Okunishi, A. J. D'Alfonso, N. R. Lugg, L. J. Allen and P. D. Nellist, *Ultramicroscopy*, 2013, **133**, 109–119.

37   S. Van Aert, A. De Backer, G. T. Martinez, B. Goris, S. Bals, G. Van Tendeloo and A. Rosenauer, *Phys. Rev. B*, 2013, **87**, 064107.

38   G. T. Martinez, K. H. W. van den Bos, M. Alania, P. D. Nellist and S. Van Aert, *Ultramicroscopy*, 2018, **187**, 84–92.

39   P. E. Greenwood and M. S. Nikulin, *A Guide to Chi-Squared Testing*, Wiley, New York, 1996.

40   F. F. Krause, M. Schowalter, T. Grieb, K. Müller-Caspary, T. Mehrtens and A. Rosenauer, *Ultramicroscopy*, 2016, **161**, 146–160.

41   I. Lobato and D. Van Dyck, *Ultramicroscopy*, 2015, **156**, 9–17.

42   I. Lobato, S. Van Aert and J. Verbeeck, *Ultramicroscopy*, 2016, **168**, 17–27.

43   J. Rodriguez-Carvajal, *Phys. B*, 1993, **192**, 55–69.
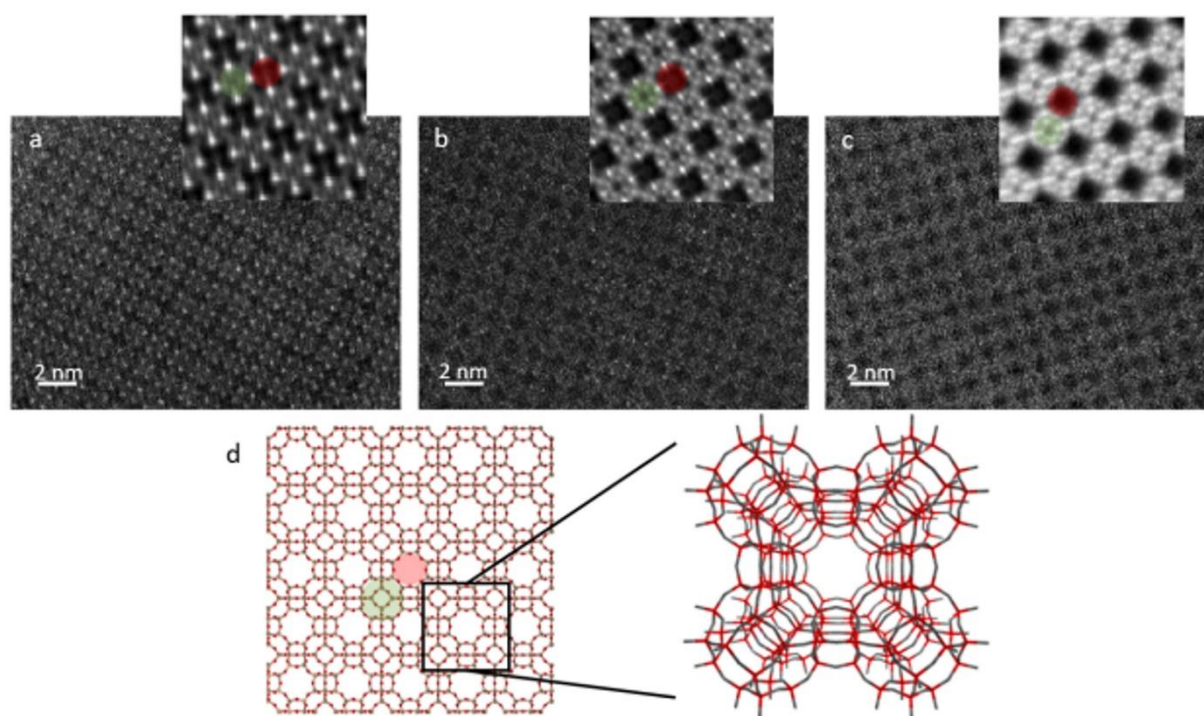
Figure 1. Examples of high-resolution HAADF STEM images of (a) over-exchanged Pb-LTA, (b) Pb_1-LTA, and (c) $Pb_{0.5}$-LTA zeolites acquired along the [100] zone axis. The insets show averaged images resulting from template matching. (d) Schematic showing the LTA zeolite structure projected along the [100] zone axis, including a three-dimensional representation of the highlighted area. Supercages and SOD cages have been indicated in red and green, respectively.
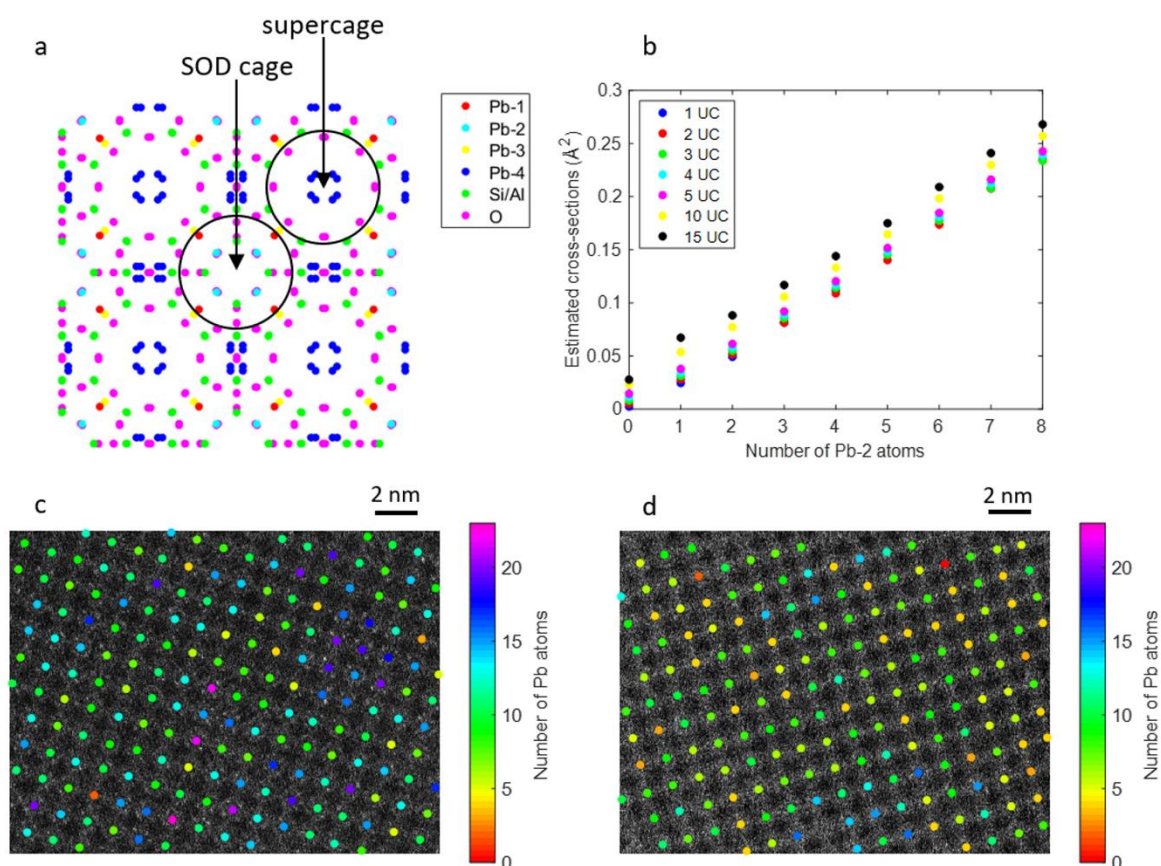
Figure 2. (a) The Pb-LTA zeolite UC with a size of 2.44 nm, centered around a SOD cage, viewed along the [001] zone axis. (b) Estimated cross-sections of a Pb-2 column from simulated HAADF STEM images as a function of number of Pb atoms for varying surrounding zeolite thickness expressed in terms of number of UCs. (c) and (d) Examples of high-resolution HAADF STEM image data, corresponding to Figures 1(b) and (c), of Pb_1-LTA and $Pb_{0.5}$-LTA zeolites, respectively, superimposed with the total estimated number of Pb atoms of the SOD cages observed along the [100] direction. In (c), the average number of Pb atoms per projected SOD cage along the [100] direction equals 0.9 ± 0.2 atoms, whereas in (d), this is 0.6 ± 0.2 atoms.
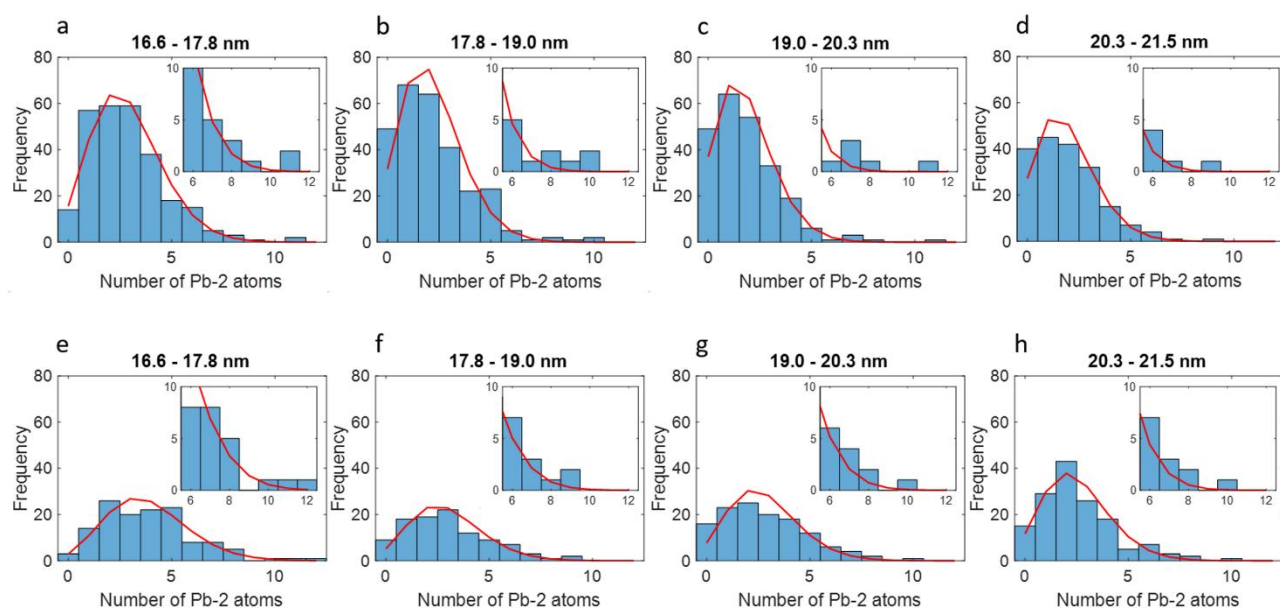
Figure 3. Histograms showing the observed distributions of the number of Pb-2 atoms along the viewing direction of projected SOD cages for different thicknesses, indicated above the plots, of the Pb_1-LTA zeolite sample in (a)-(d) and the $Pb_{0.5}$-LTA zeolite sample in (e)-(h). The red curves correspond to Poisson distributions indicating the expected distributions if the positioning of the Pb atoms would be a random process. For (a)-(d), the mean λ of the Poisson distributions equals 2.86, 2.17, 1.83, and 1.93 atoms, respectively, whereas for (e)-(h), this is 3.83, 2.98, 2.80, and 2.54 atoms, respectively. The tails of the distributions are enlarged in the insets.
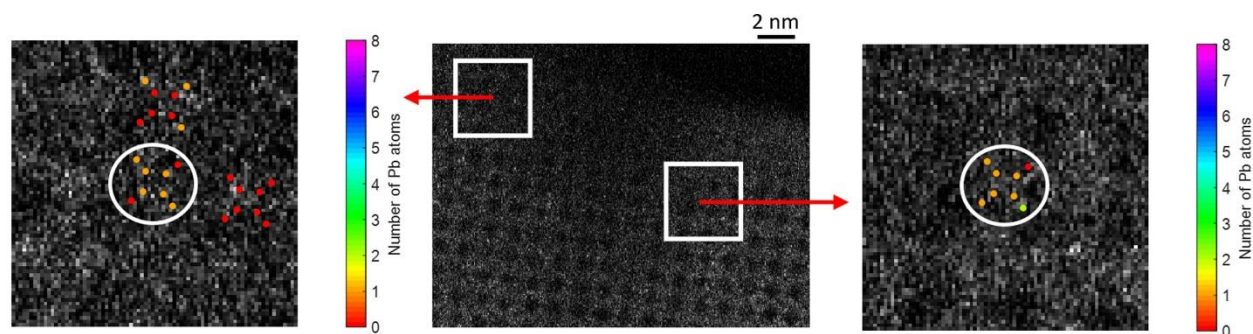
Figure 4. High-resolution HAADF STEM image of the $Pb_{0.5}$-LTA zeolite sample acquired along the [100] zone axis where areas containing possible Pb clusters inside SOD cages have been indicated. At the left-hand side, a possible tetrahedral Pb-cluster has been highlighted, surrounded by 2 Pb atoms, observed along an estimated sample thickness of 4.0 nm. At the right-hand side, a similar candidate cluster is shown for an estimated thickness of 5.9 nm. For clarity, the atom-counting results of the closely located Pb-1 and Pb-3 positions in the image plane (see Figure S2) have been merged.

Pb atom positions	Occupancy in Pb$_1$-LTA (TEM)	Occupancy in Pb$_{0.5}$-LTA (TEM)	Occupancy in over-exchanged Pb$_{full}$-LTA (TEM)	Occupancy in over-exchanged Pb$_{full}$-LTA (XRD)
Pb-1	0.3773 ± 0.0021	0.3061 ± 0.0019	0.3117 ± 0.0058	0.2486 ± 0.002
Pb-2	0.1827 ± 0.0010	0.3221 ± 0.0019	0.1703 ± 0.0037	0.1972 ± 0.001
Pb-3	0.2804 ± 0.0011	0.1506 ± 0.0017	0.4835 ± 0.0094	0.5241 ± 0.002
Pb-4	0.1596 ± 0.0010	0.2211 ± 0.0018	0.0347 ± 0.0007	0.0301 ± 0.0004

Table 1. Normalized occupancy factors of the different Pb positions within Pb$_1$-LTA, Pb$_{0.5}$-LTA and Pb$_{full}$-LTA zeolites obtained from HAADF STEM. For the Pb$_{full}$-LTA sample, the normalized occupancy factors obtained from XRD are given as well. Occupancy values normalized by the sum of individual occupancies.
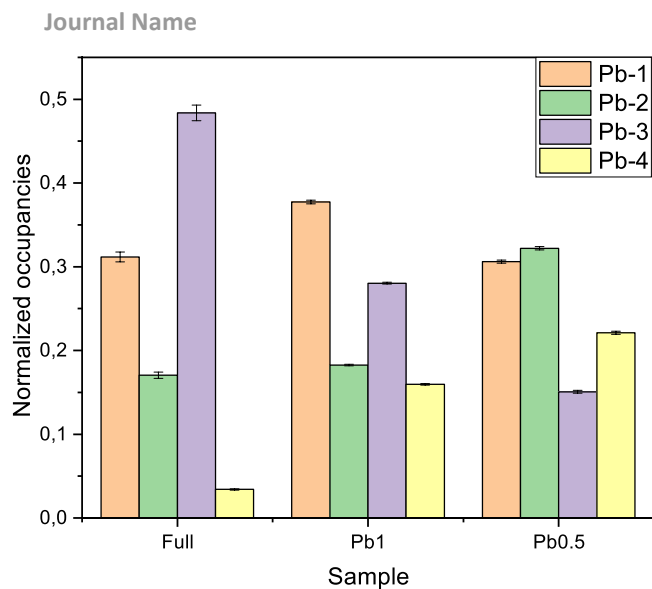
Figure 5. Graphical representation of normalized occupancies calculated from HAADF STEM images.